Modeling underground climate change across a city based on data about a building block

Zhonghao Chu¹ and Alessandro F. Rotta Loria^{1,*}

¹Northwestern University, Department of Civil and Environmental Engineering,

Subsurface Opportunities and Innovations Laboratory, 2145 Sheridan Road, Evanston-60208, IL, USA

*Corresponding author: af-rottaloria@northwestern.edu

Subsurface heat islands induce an underground climate change in urban areas, which can threaten

public comfort and health, subsurface ecosystems, transportation infrastructure, and civil

infrastructure. Meanwhile subsurface heat islands harbor a marked energy recovery potential.

Despite increasing investigations, the understanding of subsurface heat islands remains limited and

suffers from the lack of expedient and accurate simulation approaches. Here we explore the use of

machine learning to accurately and expediently simulate subsurface heat islands in terms of ground

temperature and deformation anomalies. Using the Chicago Loop district as a case study, we identify

a series of physical features to establish a relationship between central drivers and effects of

subsurface heat islands. We incorporate these features into a random forest model to simulate

underground climate change with variable training datasets. The results indicate that ground

temperature and deformation anomalies across an entire city district can be predicted based on data

extracted solely from a handful of buildings. The proposed approach achieves comparable accuracy

to current simulation methods but boasts a calculation speed that is over a hundred times faster,

promising to advance fundamental science while effectively informing engineering and decision-

making in the mitigation of underground climate change.

Key words: Urban climate; Heat islands; Subsurface; Machine learning; Random forest

1

1. Introduction

Urban heat islands (UHIs) refer to the occurrence of higher temperatures in urban areas than surrounding rural areas (Oke et al., 2017). Over the past forty years, surface (i.e., atmospheric) UHIs have been extensively studied (Debbage & Shepherd, 2015; Heaviside et al., 2017; Kalnay & Cai, 2003; Oke et al., 2017; Rizwan et al., 2008), focusing on central causes, patterns, and impacts of such pervasive phenomena. Despite these advances, investigations have recognized only recently that UHIs also extend into the subsurface (with a higher intensity and diffusion rate), resulting in subsurface urban heat islands (SUHIs) (Ferguson & Woodbury, 2007; Menberg et al., 2013).

SUHIs are primarily driven by the rejection in the urban underground of vast quantities of waste heat deriving from anthropogenic heat sources (Noethen, Hemmerle, & Bayer, 2023), such as building basements (Bidarmaghz et al., 2019), underground parking garages (Noethen, Hemmerle, Menberg, et al., 2023) and tunnels (Rotta Loria et al., 2022), resulting in an underground climate change (Rotta Loria, 2023). These phenomena have multiple adverse effects on urban systems. As ground temperature increases, the local diversity of plants and invertebrates decreases (Robinson et al., 2018). Moreover, ground warming can accelerate the decomposition of soil and rock organic carbon, leading to increased carbon dioxide emissions (Knorr et al., 2005). Ground temperature rises also promote bacterial growth in shallow water pipelines, posing a contamination risk (Müller et al., 2014). Extreme temperatures in underground transportation systems and structures can additionally result in thermal discomfort and heat-induced diseases for passengers and represent an issue for the operation of transportation networks (Jenkins et al., 2014). Furthermore, temperature variations in the urban underground due to SUHIs cause thermally induced ground deformations that have been shown to be potentially detrimental for the serviceability of civil infrastructure (Rotta Loria, 2023). Meanwhile, SUHIs offer an opportunity to reutilize substantial amounts of heat via geothermal technologies, thereby representing a highly compelling solution to reduce the

unwanted negative effects of subsurface temperature rises (Bayer et al., 2019; Benz et al., 2022; Zhu et al., 2010).

As a result of the increasingly pervasive and significant impacts of SUHIs on urban systems, the study, simulation, and prediction of UHIs and SUHIs are utmost priorities across science, engineering, technology, and decision-making for the ultimate conservation of cities. Both UHIs and SUHIs can be studied through various types of field measurements and computational simulations. However, the exploration and modeling of SUHIs are inherently more daunting than UHIs, mainly because the drivers and effects of the former are more difficult to characterize compared to the latter.

An established approach to study UHIs consists of satellite imagery (e.g., MODIS (Clinton & Gong, 2013) and Landsat (Yuan & Bauer, 2007)). However, such an approach is inapplicable to gather data about the underground. Digital information collected for the urban surface may be used to derive data for the subsurface via inverse modeling approaches (Zhan et al., 2014; Benz et al., 2016; Hemmerle et al., 2019; Huang et al., 2020), but these approaches remain in their infancy. In situ measurements are widely employed to study UHI (Oke et al., 2017) and find increasing applications for the analysis of SUHIs via the use of loggers (Noethen, Hemmerle, Menberg, et al., 2023), monitoring wells (Alberto & Crosta, 2021; Epting & Huggenberger, 2013; Ferguson & Woodbury, 2007; Menberg et al., 2013; Schweighofer et al., 2021; Taniguchi et al., 2007), or boreholes/stations (Müller et al., 2014; Shi et al., 2012; Lokoshchenko & Korneva, 2015; Luo & Asproudi, 2015; Bayer et al., 2016). However, the related SUHI studies inherently suffer from a coarse spatial resolution due to a limited number of measurement points, which are selected opportunistically rather than scientifically (Oke et al., 2017) and at the expense of marked costs linked to the underground explorations. Notably, both satellite imagery and in situ measurements can underpin the study of UHIs and SUHIs but neither of these approaches allow to simulate and predict such pervasive phenomena.

Computational simulations are the premier approach enabling not only the study but also the simulation and prediction of both UHIs and SUHIs. Computational simulations of UHIs uniquely provide high-resolution information across multiple scales, ranging from individual buildings to entire cities (Oke et al., 2017), and customarily resort to computational fluid dynamics, finite element (FE), or mixed simulations (Rizwan et al., 2008). Recently, FE simulations have also been exploited to study SUHIs (Bidarmaghz et al., 2019; Rotta Loria, 2023; Epting & Huggenberger, 2013; Visser et al., 2020; Previati et al., 2022; Kreitmair et al., 2023). Based on mathematical formulations that can leverage a variety of couplings between central physical phenomena linked to the spread and effects of urban heat, FE simulations can provide a thorough understanding of the mechanisms underlying SUHIs, and they are also highly accurate for modeling complex geometries and boundary conditions. However, such computational approaches require significant expertise, computational facilities, and time to be performed, which are often unavailable. Additionally, while the necessary data for computational simulations of UHIs (e.g., about the urban geometry and morphology, or the drivers of heat islands) are generally readily available, those required for the study of SUHIs are more difficult to obtain (D. Zhou et al., 2019). This evidence not only complexifies any simulation of SUHIs but often requires sensitivity analyses to soundly assess the variability of simulation results based on limited input datasets, making the overall study of SUHIs daunting.

In light of the shortcomings in existing approaches to studying, simulating, and predicting UHIs and SUHIs, there is a sense of urgency and a compelling opportunity to develop innovative auxiliary investigation and modeling tools. Machine learning (Hastie et al., 2009; Zhou, 2021) (ML) emerges as a transformative means for the investigation, simulation, and prediction of problems across various domains, involving teaching machines to learn from data and make predictions based on patterns and insights. Its advantages lie in automating processes, improving efficiency, and enabling systems to adapt and improve with experience. However, ML may lack physical interpretability and is often heavily dependent on the quality and quantity of the training data. Nevertheless, compared to FE methods, ML approaches are computationally efficient and quick to run, especially for long-term simulations that are necessary to

comprehensively investigate the impacts of UHIs and SUHIs. In recent years, ML has demonstrated outstanding simulation and prediction capabilities in studying UHIs. However, due to differences in the heat transfer mechanisms above and below the ground, existing ML approaches proposed for UHI studies (Gobakis et al., 2011; Kafy et al., 2021; Mushore et al., 2017; Papantoniou & Kolokotsa, 2016; Zumwald et al., 2021) are unsuitable for analyzing SUHIs. A recent study based on statistical clustering has been proposed to reduce the computational cost of FE simulations and obtain high-fidelity models to analyze SUHIs (Kreitmair et al., 2023). Despite this advancement, there seemingly are no investigations that harness ML for the study, simulation, and prediction of SUHIs.

This work unprecedently presents a ML approach for the study, simulation, and prediction of SUHIs. Specifically, this work harnesses the random forest (RF) algorithm to address the question: can we accurately and efficiently predict underground climate change across entire cities over long timeframes based on data collected around a handful of buildings over short timeframes? We chose as reference for this study a high-resolution grid of 5×5 m "urban elements" (which correspond to zones of uniform properties in the studied urban area) and a simulation timeframe of 100 years – from 1951 to 2051. Then, based on the identification of physically based features, we train the RF algorithm by using the results of experimentally validated FE simulations (Rotta Loria, 2023). Such training is performed with reference to three input datasets of variable density of information, which enables us to simulate underground climate change in space and time domains. By comparing 2-D maps of ground temperature and strain anomalies with those achieved with the reference FE simulations (Rotta Loria, 2023), we affirmatively answer to the question set by this work. Subsequently, we broaden our analysis by exploring the influence of varying urban morphologies on the intensity of SUHIs—an aspect seemingly overlooked to date considering that most of current studies are conducted by modeling a specific urban morphology (e.g., Basel (Epting & Huggenberger, 2013), London (Bidarmaghz et al., 2019), Munich (Böttcher & Zosseder, 2022), and Chicago (Rotta Loria, 2023)). Finally, we critically discuss the capabilities of the proposed modeling approach, whose future use has the potential to advance the current scientific understanding of SUHIs and

other problems involving the diffusion of heat in the subsurface, while also contributing to engineering and decision-making actions to control such pervasive phenomena.

2. Methodology

2.1 Case study

The case study selected for this work consists of the Chicago Loop district: the downtown business district of Chicago. The features of such urban area are presented in detail elsewhere (Cassina et al., 2022), together with recent experimental evidence about the presence of an intense SUHI (Rotta Loria et al., 2022). Therefore, here we recall only essential information for the sake of the present work. The local soil stratigraphy consists of sand and clay layers with highly variable properties resting on a bedrock (Table 1). The undisturbed ground temperature in the Loop is $T_0 = 11.2$ °C. Overall, there are four main types of underground heat sources across the district: building basements, parking garages, subway tunnels, and a train station. As for parking garages, there are four, i.e., Grant Park North (GPN), Grant Park South (GPS), Millennium Park Garage (MG) and Lakeside Garage (LG), with different monthly average temperatures for each one.

Table 1: Properties of the ground underneath the Chicago Loop used in FE simulations. The depth z is positive going downwards.

G 1 1 1	Depth	Thermal	Crasifia haat a	Density,	Young's	D-!	Linear
Geological	range, z	conductivity, λ		ho [kg/	modulus,	Poisson's	thermal
layer	[m]	[W /(m ° C)]	[J/(kg°C)]	m ³]	<i>E</i> [MPa]	ratio, ν [-]	expansion

							coefficient, α
							[1/°C]
Sand	$0 \le z \le 4$	1	782	1918	31	0.2	1.0 × 10 ⁻⁵
Soft clay	$4 \le z \le 16$	1.22	1456	1846	10	0.2	-9.0×10^{-6}
C4:00 -1	16 ≤ <i>z</i> ≤	1.22	1456	2000	2.1	0.2	0.0 × 10-6
Stiff clay	19	1.22	1456		31	0.2	-9.0×10^{-6}
Hond alors	$19 \le z \le$	1.22	1456	2081	214	0.2	9.0 × 10-6
Hard clay	27	1,22	1430			0.2	9.0 ^ 10-0
Sand and	$27 \le z \le$	3	1035	2320	75	0.2	1.0 × 10-5
boulders	34	3	1033	2320	13	0.2	1.0 ^ 10-3
Dolomitic	$z \ge 34$	3	835	2639	45, 586	0.1	2.2 × 10-6
limestone	2 ≥ 34	3	633	2039	75, 500	0.1	2.2 ^ 10-0

2.2 FE simulations

FE simulations harnessing a 3-D model of the Chicago Loop and informed and validated by experimental data (Rotta Loria et al., 2022) have been recently presented to explore the SUHI in such urban area (Rotta Loria, 2023). Therefore, they represent a valuable source of reference data for the training and validation of the proposed ML approach. Notably, here the FE simulations use the same model but resort to a simplified mathematical formulation that omits the influence of the limited groundwater flow in the considered area. This choice is made to expedite the FE simulations that were run to underpin the analyses presented in this work. Its adequacy is corroborated by the close comparison between the obtained results presented in this work and the reference study (Rotta Loria, 2023). Other than this difference, the modelling approach, including the initial and boundary conditions employed, coincide with those detailed in the reference study (Rotta Loria, 2023). Essentially, the FE simulations simulate across the considered urban

area the rejection of heat from underground structures and the ground surface into the subsurface and the resulting impacts of temperature variations on the mechanics of the ground.

The area of interest spans across 2400 m \times 2200 m. The reference simulation time ranges from 1951 to 2051, i.e., 100 years. In this timeframe, we mainly concentrate on the years 1952, 2022, and 2051. These dates correspond to specific simulation times: t = 1 year after the completion of the subway system in 1951, when according to historical data the number and location of infrastructures in the Chicago Loop remained relatively stable till the present time (Rotta Loria, 2023); t = 71 years of subsequent heat diffusion from underground structures into the ground, which led to marked temperature anomalies recently measured on site (Rotta Loria et al., 2022); and t = 100 years, corresponding to a prediction for approximately the next 25 years. The FE simulations (similar to the corresponding ML simulations) approximately consider that all building start to reject heat into the ground from the same time (1951), as if they were constructed in a unique occurrence. Although approximate, this choice provides simulation results that closely match with recently measured temperature anomalies in the considered urban district (Rotta Loria, 2023), proving the adequacy of such simplification.

The analyses presented here consider the geomechanics sign convention as reference. Accordingly, contractive strains are considered positive, while expansive strains are considered negative.

2.3 Random forest algorithm

In this study, the random forest algorithm is used for analysis in Python. RF is an ensemble of decision trees. At each node, there are a series of binary splits that separate the training data into two child nodes according to one feature and a true/false question. For regression tasks, the mean prediction of the individual trees is returned (Ho, 1995), which is also called "bagging". RF offers several advantages, prominently emphasizing its capability to handle large datasets with high dimensionality, mitigate overfitting, and

deliver robust predictions. It significantly enhances the model's accuracy and generalization performance, particularly showcasing its prowess in capturing non-linear relationships within the data (Breiman, 2001; Hastie et al., 2009).

2.3.1 Urban area discretization

With the selected algorithm, our goal is to simulate and predict the temperature and thermally induced vertical strain fields that characterize the ground over the considered urban area. As we aim to address this challenge with a high resolution, we discretize reference cut planes of interest across the Chicago Loop in a grid of 5 m × 5 m "urban elements", hence creating a grid of 211,200 elements. For ease of extracting coordinate information, we discretize all heat sources (i.e., building basements, parking garages, tunnels and the train station) into rectangular shapes through segmentation and approximation. We consider that the upper boundaries of the heat sources coincide with the ground surface. Meanwhile, the lower boundaries extend underground at varying depths representative of reality (Rotta Loria, 2023).

2.3.2 Features

In ML simulations, features are the variables (or attributes) used to represent data, and play a fundamental role in the training of algorithms. In this study, we select physically based features to help the selected ML algorithm learn as efficiently and effectively as possible from the provided data. The overarching consideration behind the selected features is that the heat transfer and deformation phenomena caused by SUHIs inherently depend on the urban morphology of cities and hence on the location of heat sources, becoming less notable for given subsurface properties with increasing distances. Based on this consideration, we identify the following features for the analysis of SUHIs (Fig. 1):

- Distance from nearby heat sources ($D_{xy(i)}$ and $D_{z(i)}$). For each urban element, we select its center point as a reference point. Starting from this point, we identify the minimum distance in the horizontal direction from the reference point to the four nearest heat sources (called as HS1, HS2, HS3, and HS4) as a set of four features (denoted as $D_{xy(1)}$, $D_{xy(2)}$, $D_{xy(3)}$, and $D_{xy(4)}$). When the centroid is within the heat source projection area, this value is set to 0. Then, we sequentially calculate the differences between the vertical coordinates of the studied plane (Z_s) and the four reference heat sources, considering them as other four features (denoted as $D_{z(1)}$, $D_{z(2)}$, $D_{z(3)}$, and $D_{z(4)}$). We acknowledge that the consideration of four heat sources is arbitrary and other numbers may be considered. We chose this specific number for this study due to the proximity of underground heat sources across the Chicago Loop. Other number of heat sources may indeed be considered. We leave this aspect to numerical modelers interested in other urban areas, with the premises that the selected feature does represent an effective variable to train ML algorithms.
- Number of heat source projections (N_i) in the horizontal direction within given radii of influence (R_i). For each urban element, we further assess the proximity of heat sources by considering as reference their projections in the horizontal direction as a feature. The number of heat source projections is considered as a feature because, at any given depth in an urban area, the ground zones affected by the most significant temperature and strain anomalies are approximately located beneath the influencing heat sources, which leave an "imprint" in the ground. For any studied plane, we thus project all heat sources onto it. Subsequently, for the centroid of each element on that plane, we define three influence radii, examining the number of heat source projections within each influence radius. The influence radii correspond to $R_1 = 5$ m, $R_2 = 10$ m, and $R_3 = 15$ m (i.e., a distance amounting to one urban element width, twice such width, and three times such width). Again, we acknowledge that the consideration of three radii of influence with the values proposed here is arbitrary and other numbers may be considered. However, this number of influence radii

has been found to result in predictions characterized by an optimum balance between accuracy and efficiency. Meanwhile, the three values of the influence radii may be considered inclusive of multiple buildings in dense urban areas, being proportional, if not coincident, to the width of typical streets and building footprint. Therefore, these features promise to represent valuable attribute to train ML algorithms for the study of general urban areas.

- Horizontal heat source projection coverage ratio (S_{PCR}) . For each element, we calculate the ratio of the area covered by heat source projections (S_{HSP}) on the studied plane to its total area (S_{Total}) . This feature measures the extent to which the element is directly influenced by the heat source located directly above.
- Weighed temperature (T_j) within given influence radii. This feature considers the influence of temperatures of surrounding heat sources. For each type of heat source, we first define its annual average temperature as its feature temperature. Then, we calculate the weighted temperature of each element within the three influence radii $R_1 = 5$ m, $R_2 = 10$ m, and $R_3 = 15$ m as follows:

$$T_j = T_0 + \frac{\sum_{i=1}^{N_j} \frac{T_{HS}(i)}{r_i}}{\sum_{i=1}^{N_j} \frac{1}{r_i}}, \text{ where } j = 1, 2, 3$$
 (1)

where the temperature within each influence radius is weighted by the reciprocal of the horizontal distance (r_i) from each heat source within this radius to the element center point. $T_{HS}(i)$ is the feature temperature of i-th heat source within a given influence radius (i.e., an arithmetic mean). Obviously, if there is no heat source within a given radius of interest, the weighed temperature corresponds to the initial temperature T_0 .

- Temperature of urban elements ($T_{element}$). When predicting thermally induced ground strains, we incorporate the temperature of each element as a feature to enhance accuracy.
- *Time (t)*. For predictions in the time domain, we include time as an extra feature, as heat transfer and deformation process inherently vary as a function of time.

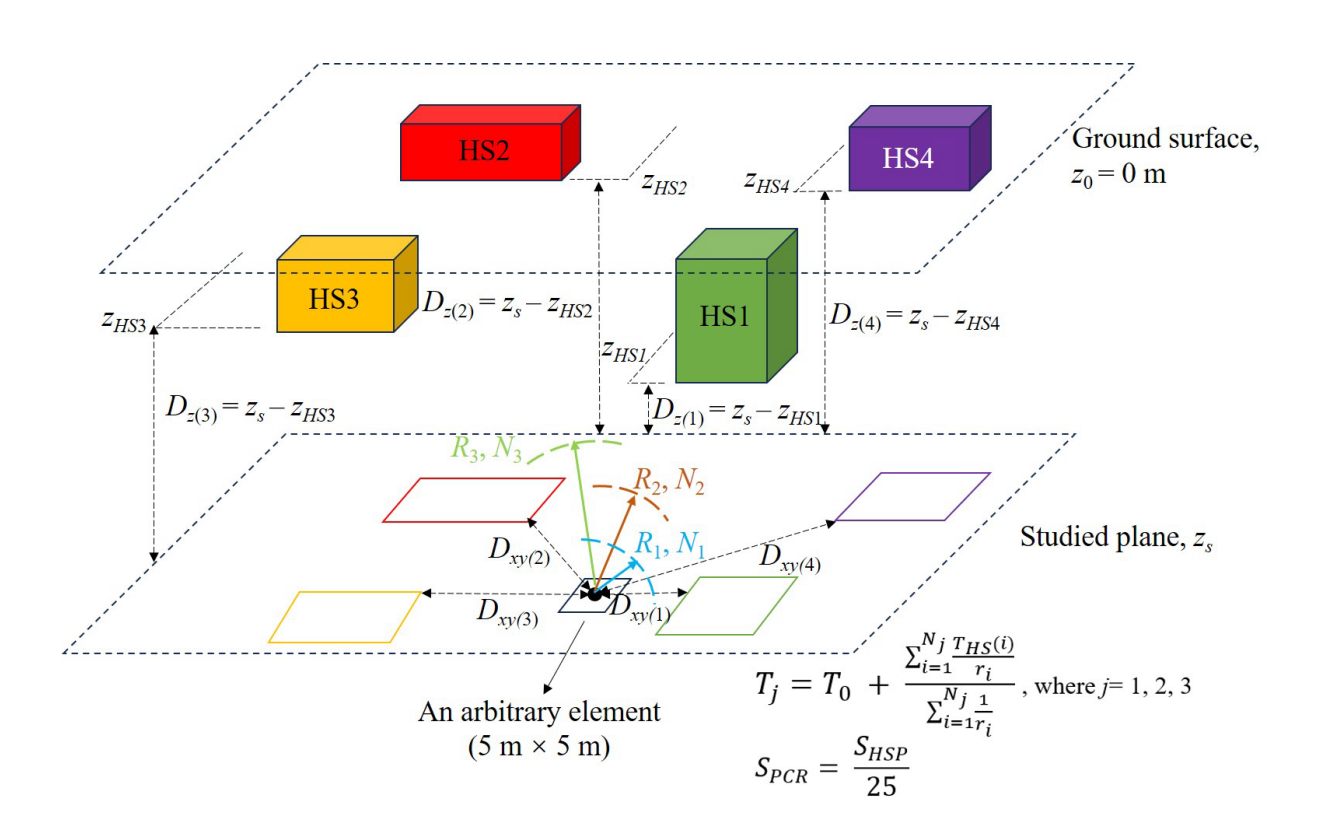


Fig. 1: Features allowing the data-driven prediction of SUHIs. $D_{xy(i)}$ and $D_{z(i)}$ (i = 1, 2, 3, 4) are the horizontal and vertical distances from the reference point of any considered element to the four nearest heat sources (represented as HS1, HS2, HS3, and HS4). N_i is the number of heat source projections in the

horizontal direction within given radii of influence R_i (i = 1, 2, 3). S_{PCR} is the horizontal heat source projection coverage ratio. T_i is the weighed temperature within given influence radii.

2.3.3 Training of ML simulations

The training of the ML simulations is based on the use a relatively small set of data. The primary aim of this approach is to predict the intensity and effects of SUHIs expediently and accurately, while avoiding the significant costs of FE simulations. For each specific depth, we extract three distinct training datasets, labeled A, B, and C: (A) a random selection of 20% of the available urban elements, corresponding to about 15% of the studied area (i.e., the area of 2400 m × 2200 m); (B) data collected beneath different types of underground infrastructure (Table 2), corresponding to about 0.9% of the available elements and 0.7% of the studied area; and (C) data gathered around only one building block, corresponding to about 0.5% of the available elements and 0.4% of the studied area (i.e., Area 1 in Table 2).

Table 2: Composition of training datasets B and C. The origin of the coordinate system (x = 0, y = 0, z = 0) is in the southwestern corner of the ground surface in the model. The positive direction of the x-axis is from west to east. The positive direction of the y-axis is from south to north. The positive direction of the z-axis points from the ground surface downwards.

Area number	Training dataset label	Number of elements	Area range (horizontal) [m]	Corresponding heat source
1	B, C	840	$1020 \le x \le 1170, 1390 \le y \le 1530$	One building block
2	В	144	$1230 \le x \le 1320, 1525 \le y \le 1565$	Small blocks of Grant Park North and METRA station
3	В	24	$1250 \le x \le 1265, 1050 \le y \le 1090$	One small block of Grant Park South
4	В	162	$410 \le x \le 500, 2055 \le y \le 2100$	One small portion of the CTA subway (blue line)
5	В	112	$880 \le x \le 900, 1090 \le y \le 1230$	One small portion of the CTA subway (red line)
6	В	100	$1500 \le x \le 1550, 700 \le y \le 750$	An area of green space (no heat sources)
7	В	144	$1670 \le x \le 1730, 1500 \le y \le 1560$	One small block of Lakeshore Garages

2.3.4 Assessment of prediction accuracy

In this work, we employ mean absolute error (MAE), mean absolute percentage error (MAPE) and coefficient of determination (R^2) as metrics to assess the performance of the proposed ML model. Their expressions are:

$$MAE = \frac{1}{n} \sum_{i=1}^{n} (Y_i - \hat{Y}_i)$$
 (2)

$$MAPE = \frac{1}{n} \sum_{i=1}^{n} (Y_i - \hat{Y}_i) \times 100\%$$
 (3)

$$R^2 = 1 - \frac{Sum \ of \ squared \ residuals}{Total \ sum \ of \ squares} \tag{4}$$

where n is the number of samples, Y_i is the true value, and \hat{Y}_i is the predicted value by the ML algorithm. The "sum of squared residuals" is the sum of the squared differences between the actual and predicted values, whereas the "total sum of squares" is the sum of the squared differences between the actual values and their mean.

When calculating the selected metrics to assess the simulation accuracy with respect to temperature, we only include urban elements with temperatures above 11.2 °C (i.e., where the temperature anomaly with respect to the initial conditions is larger than zero), as our focus is on the warming areas affected by SUHIs. Additionally, given that the range of strains is considerably larger than that of temperatures, we adopt an ad-hoc approach for evaluating effectively the selected performance metrics for the strains. For a given depth, we calculate the performance metrics only for strain values $|\varepsilon| \ge 1/10$ of the maximum strain under free deformation conditions (i.e., $|\varepsilon| \ge |\alpha \Delta T_{max}|/10$), where ε represents thermal strain, α is the thermal expansion coefficient, and ΔT_{max} is the maximum temperature increment at that depth.

3. Results

3.1 Predictions in the space domain

In this section, we investigate the ability of the proposed ML approach to simulate the ground temperature and strain contours in the middle of selected soil layers in the studied urban area (sand layer -z = 10 m; stiff clay layer -z = 17.5 m; hard clay layer -z = 23 m) (Fig. 2 and Fig. 3). Specifically, we train the ML algorithm with data referring to a limited set of spatial coordinates at given time intervals to study SUHIs in broader locations of interest at the same time intervals. Appendix Fig. 5 and Fig. 6 provide additional results; Appendix Table 4 and

Table 5 show the errors of all the studied cases.

The ML simulations provide ground temperature anomalies that match overall very well with those quantified through the FE simulations (Fig. 2). Temperature anomalies become more pronounced as closer spatial coordinates to heat sources (e.g., underground structures) and longer times of heat rejection in the ground are considered. Temperature anomalies also become more pronounced in areas characterized by larger and denser heat sources, reflecting a strong dependence of the intensity of SUHIs on urban morphology. The ML simulations using training datasets corresponding to 15% (i.e., set A) and 0.7% (i.e., set B) of the studied area provide close predictions of the temperature anomalies resulting from FE simulations at the depth of z = 10 m and for the recent year 2022 (Fig. 2(a)). Such results particularly exhibit MAE of 0.28°C and 0.46°C and MAPE of 1.9% and 3.2% with coefficients of determination $R^2 = 0.95$ and 0.90, respectively. As training set B includes multiple types but very few heat sources, it results in slightly lower accuracy compared to set A. Nonetheless, the obtained discrepancies between the modeled and predicted results appears minimal in all cases, not only for scientific purposes but also for engineering purposes and decision-making. Multiple reasons can be identified to justify the acceptability of the obtained results. First, discrepancies between predicted and modeled (or measured) temperature anomalies of a few tens of Celsius are of the same order of magnitude of the accuracy characterizing widespread temperature sensors that may be used to validate simulation endeavors deriving from FE or ML approaches. Second, inaccuracies in the definition of temperature anomalies amounting to a few Celsius are set to minimally impact the quantifications of heat flows and deformations caused by SUHIs, which are generally of interest to analyze such phenomena from energy and civil engineering perspectives. Third, the foregoing inaccuracies are deemed limited given the complexity of subsurface environments (especially compared to surface environments) and the inherent variability that characterizes analyses of such problems. Notably, in another study leveraging ML to analyze Chicago's surface air temperature (Lyu et al., 2022), a MAE of 0.79 °C, 0.78 °C, and 0.46 °C was obtained over three consecutive years. In a further study (Amato et al., 2020), a MAE of 1.15 °C was reported. Based on all of these considerations and results, the errors in this study are considered acceptable.

The ML simulations using the largest training dataset achieve the highest prediction accuracy. Those using the intermediate training set also yield satisfactory results, albeit with a reduced accuracy. In contrast, the ML simulations using the smallest dataset corresponding to 0.4% of the studied area (i.e., set C) exhibit a larger *MAE* of up to about 1°C (Fig. 2(a)). Notably, the *MAE* of such simulations is minimal underneath building basements, whereas it becomes significant in ground areas influenced by other types of heat sources, such as underground parking garages. This result is due to the fact that the considered ML simulations were trained with ground data gathered only from around building basements, and hence indicates that the nature of the training dataset influences the accuracy of the output of ML simulations.

The ML simulations also match well with the FE results at a depth of 10 m in the year 1952 (Fig. 2 (b)). However, the errors obtained for the simulation time of t = 1 year (i.e., 1952) are significantly smaller than those for t = 71 years (i.e., 2022), irrespective of the employed training datasets. This result is attributed to the relatively subtle intensity of the SUHI during the early activation of the heat sources and indicates a variability of the obtained results depending on the simulation time.

Highly satisfactory simulations of temperature data are not only achieved at the depth of 10 m, but also at deeper depths of z = 17.5 m (Fig. 2(c)) and z = 23 m (Fig. 2(d)) in the year 2022. However, the MAEs for deeper depths are slightly larger compared to those characterizing the shallower depth, while remaining limited and valuable for both scientific and engineering purposes. This evidence indicates a variability of the obtained results depending on the distance considered from the heat sources.

Consideration of the average temperature trend of the entire subsurface of the Loop over 100 years at three different depths provides further evidence of the capability of ML simulations to provide comparable results to FE simulations (Fig. 2(e)). The results of ML simulations employing training datasets referring to 15% and 0.7% of the studied area closely overlap with those of FE simulations, whereas larger differences characterize ML simulations employing a training dataset corresponding to 0.4% of the studied area. Despite these differences, both the FE and ML simulations unequivocally unveil a clear feature of

underground climate change: the average ground temperature increases particularly at shallow depths closer to the higher density of heat sources, reaching a quasi-steady thermal state at a faster rate compared to depths located farther away from the heat sources. As time progresses, the average ground temperature across the considered district at selected depths tends to different values depending on the reference depth. After t = 100 years of heat dissipation from underground heat sources, the average ground temperature increases by 3.6, 3.3, and 2.9 °C at depths of 10, 17.5, and 23 m compared to the undisturbed ground temperature of 11.2 °C, respectively; meanwhile, the ground temperature in localized areas can achieve the extreme value of 20.1 °C, corresponding to a temperature anomaly of 8.9 °C (results based on training set B). These results underscore the pronounced intensity of SUHIs, which is typically higher than UHIs (Rotta Loria, 2023).

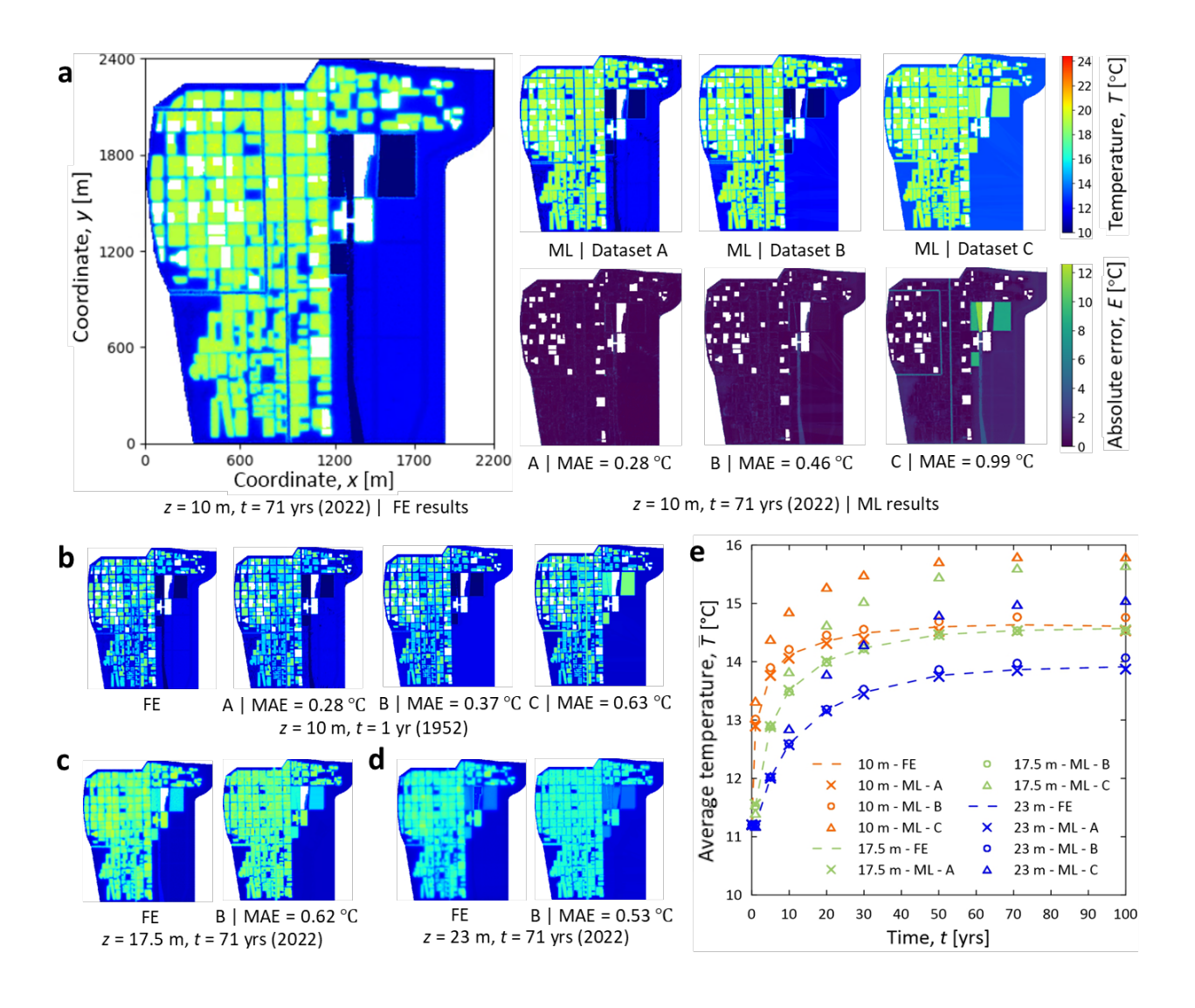


Fig. 2: Ground temperature anomalies determined by FE and ML simulations in the space domain.

(a) Temperature maps (z = 10 m, t = 71 years) obtained from the FE and ML simulations based on training sets A, B and C, and corresponding prediction errors. (b) Temperature maps (z = 10 m, t = 1 year) obtained from the FE and ML simulations based on training sets A, B and C. (c) Temperature maps (z = 17.5 m, t = 71 years) obtained from the FE and ML simulations based on training set B. (d) Temperature maps (z = 23 m, t = 71 years) obtained from the FE and ML simulations based on training set B. (e) Comparison between the average ground temperature determined via the ML and FE simulations (the temperatures deriving from the ML simulations represent arithmetic averages with respect to the total number of urban elements;

the temperatures deriving from the FE simulations represent an arithmetic average over all integration points of the planes under consideration).

The ML simulations provide thermally induced ground strains (i.e., strains caused by temperature variations) that match overall very well with those quantified through the FE simulations (Fig. 3). This result holds irrespective of whether contractive (i.e., positive) or expansive (i.e., negative) strains due to thermal collapse (Laloui, 2001; Rotta Loria & Coulibaly, 2021) and thermal expansion (Laloui, 2001; Rotta Loria & Coulibaly, 2021) are considered, respectively. Consistent with the characteristics of the temperature field, thermally induced strains become more pronounced as closer spatial coordinates to heat sources and longer times of heat rejection are considered. Thermally induced strains also become more pronounced in areas with larger and denser heat sources, reflecting a strong dependence of ground deformations caused by SUHIs on urban morphology.

The thermally induced strains quantified at a depth of 10 m for the years 2022 (Fig. 3(a)) and 1952 (Fig. 3(b)) via the ML simulations using a training dataset referring to 15% of the studied area (i.e., set A) provide results characterized by a MAE below 4 $\mu\epsilon$, whereas those resulting from simulations using training datasets referring to 0.7% and 0.4% of the studied area have MAEs under 7 $\mu\epsilon$. Considering that thermally induced ground strains can be as high as hundreds of $\mu\epsilon$ (in absolute value) near basements and other underground heat sources, the observed MAEs are minimal and largely acceptable.

As opposed to the differences between the ground temperature anomalies predicted by the ML and FE simulations, the differences between the thermally induced ground strains become smaller for increasing depths farther away from the heat sources. Specifically, the *MAE* characterizing the ML simulations deriving from training set B at depths of z = 17.5 m (Fig. 3(c)) and 23 m (Fig. 3(d)) are only 2.1 μ E and 1.4 μ E, respectively. This result arguably derives from the criterion employed to calculate the error between the simulated strain values.

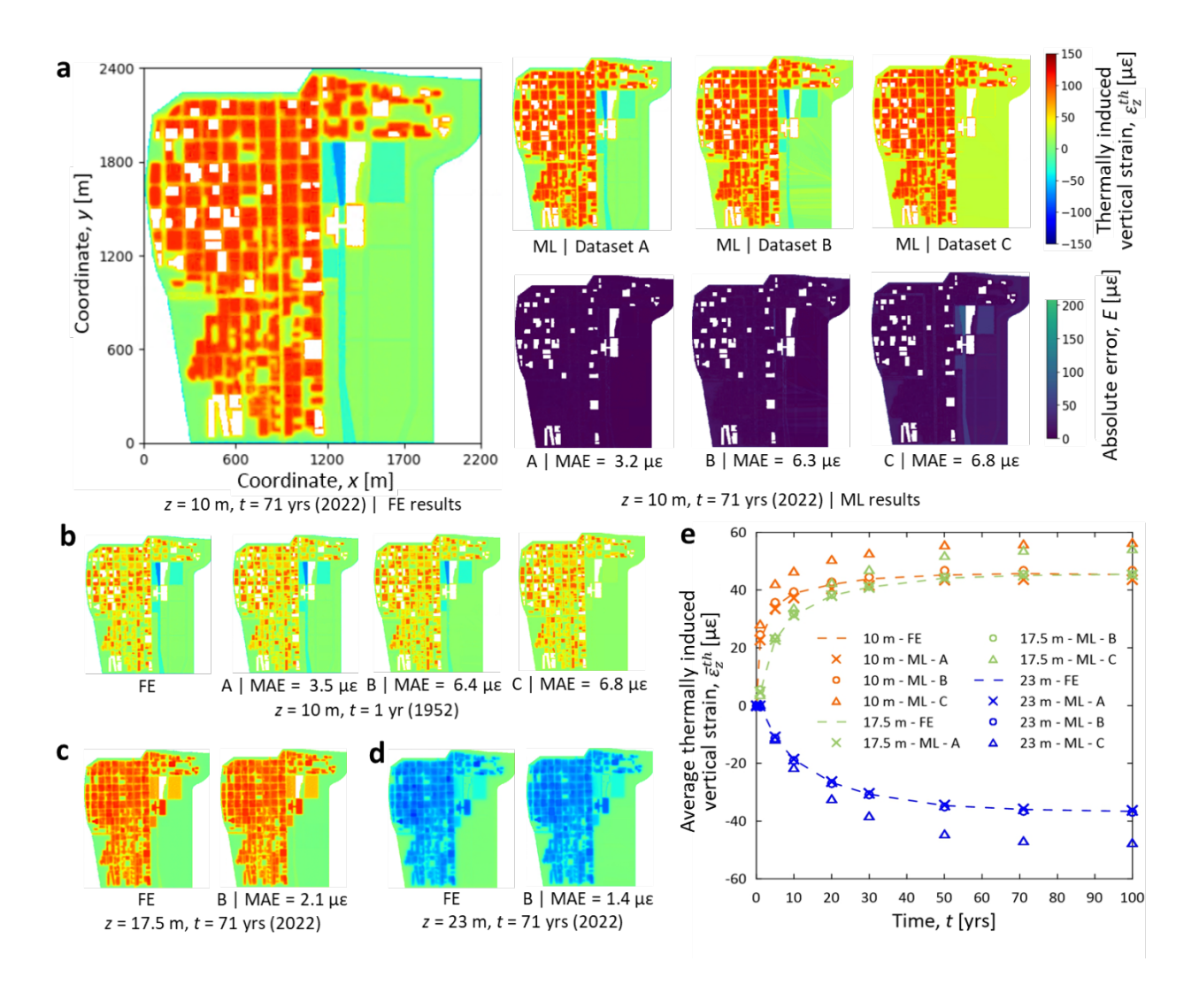


Fig. 3: Thermally induced ground strains determined by FE and ML simulations in the space domain.

(a) Strain maps (z = 10 m, t = 71 years) obtained from the FE and ML simulations based on training sets A, B and C, and corresponding prediction errors. (b) Strain maps (z = 10 m, t = 1 year) obtained from the FE and ML simulations based on training sets A, B and C. (c) Strain maps (z = 17.5 m, t = 71 years) obtained from the FE and ML simulations based on training set B. (d) Strain maps (z = 23 m, t = 71 years) obtained from the FE and ML simulations based on training set B. (e) Comparison between the average thermally induced ground strains determined via the ML and FE simulations (the strains deriving from the ML simulations represent arithmetic averages with respect to the total number of urban elements; the strains

deriving from the FE simulations represent an arithmetic average over all integration points of the planes under consideration).

Consideration of the trend of average thermally induced ground strains over 100 years highlights similar results to those obtained for the ground temperature anomalies, with closer results provided by ML simulations trained with datasets A and B as opposed to C, and the slower increase of ground deformations over time. The normally consolidated soft clay and stiff clay undergo thermal collapse (i.e., a thermally induced volumetric shrinkage) associated with the compressive strains observed at both z = 10 m and 17.5 m, which amount to approximately 45 μ s on average at t = 100 years. In contrast, the overconsolidated hard clay undergoes thermal expansion (i.e., a thermally induced volumetric expansion) associated with the negative strains observed at z = 23 m, which amount to around -36 μ s at t = 100 years. Overall, the trends of average thermally induced ground deformations determined through the ML simulations are very close to those predicted by the FE simulations and hence reliable.

3.2 Predictions in the time domain

In this section, we introduce time as a new feature to explore the potential of utilizing data collected over relatively limited timeframes to predict the effects of SUHIs effects over long timeframes. As detailed in Table 3, we consider data associated with seven sets of times ranging from the year 1951 to 2022 to simulate the effects of underground climate change in 2051 (i.e., after a heat rejection time of t = 100 years). The chosen sets of times consist of 1, 2, 3, 4, 5, 6, and 7 arbitrarily selected years. The studied effects consist of ground temperature anomalies and thermally induced strains and are simulated via different training sets (A, B, or C). Appendix Fig. 7 and Fig. 8 report all obtained results.

Table 3: MAE characterizing the ground temperature and strain determined via ML and FE simulations. Results refer to different time series and training sets.

Salasted time source	MAE o	MAE of temperature [°C]			MAE of vertical strain [με]		
Selected time series	Set A	Set B	Set C	Set A	Set B	Set C	
t = 1 yr	1.83	1.78	2.05	24.1	24.1	16.1	
t = 1 yr, 2 yrs	1.42	1.40	1.65	17.4	17.2	13.4	
t = 1 yr, 2 yrs, 10 yrs	0.61	0.62	0.80	7.4	7.3	6.8	
t = 1 yr, 2 yrs, 10 yrs, 20 yrs	0.40	0.46	0.79	5.0	5.9	6.4	
t = 1 yr, 2 yrs, 10 yrs, 20 yrs, 30 yrs	0.31	0.42	0.85	4.2	5.6	6.1	
t = 1 yr, 2 yrs, 10 yrs, 20 yrs, 30 yrs, 50 yrs	0.24	0.41	0.95	3.9	5.9	6.7	
t = 1 yr, 2 yrs, 10 yrs, 20 yrs, 30 yrs, 50 yrs, 71 yrs	0.21	0.41	0.98	3.0	5.6	6.4	

The selection of a limited number of times for the training yields larger prediction errors. For instance, when utilizing data from just one time (i.e., t = 1 year), the MAE exceeds at least 1.7 °C for the predicted temperature and at least 16 μ s for the predicted strain for the considered training sets. As we use more times to train the ML algorithm, simulations provide results characterized by a MAE that becomes consistently smaller (set A), converges toward a constant value (set B), or first decreases and then increases (set C). As a complementary piece of evidence, when we conduct the ML simulations with the three usual datasets and the consideration of the times t = 1 year, 2 years, 10 years, and 20 years (i.e., four reference years within the first 20 years to predict results over the following 80 years), all three training sets yield highly comparable results. Notably, although the consideration of one additional time (i.e., 30 years) involves better results for ML simulations trained with dataset A, marginally improves the accuracy of such results for ML simulations trained with dataset B, whereas decreases the quality of results for ML

simulations trained with dataset C. Therefore, ML simulations using training set B with a maximum time value of t = 20 years strike as the option characterized by optimal balance between accuracy and efficiency, with MAEs of 0.46 °C for temperature and 5.9 μ E for strain, and a significantly decreased computational time compared to simulations employing training set A.

A detailed analysis of the influence of the number and distribution of times used as reference for the ML simulations uncovers two noteworthy facts. On the one hand, what matters to achieve accurate ML predictions over long timeframes is not only the number but also the distribution of the times at which data are selected to train such predictions. Accordingly, predictions over 100 years can be very accurate with the selection of only four reference times when they span multiple years over at least a few decades, whereas they can be affected by significant errors when they employ reference times selected over only a decade, a year, a month, or even shorter timeframes. On the other hand, the accuracy of ML simulations quickly converges to approximately constant values for relatively limited reference times employed for the training. The optimal number of times to be considered depends on the characteristics of the broader dataset employed for the training. Here such number consists of four distinct years within a timeframe of 20 years and allows to accurately predicting results over 100 years.

3.3 Analysis of variable urban morphologies

In this section, we harness the proven abilities of the developed ML approach to capture SUHIs with the aim to explore how such phenomena intensify with the increased density of heat sources. As basements are the primary underground heat sources in the Chicago Loop, we explore the effects of basement density on ground temperatures and thermally induced strains by considering three hypothetical scenarios where a random selection of 25, 50, and 75% of the existing basements rejects heat into the ground (Fig. 4). The ML simulations harness training set B with the times t = 1 yr, 2 yrs, 10 yrs, and 20 yrs due to their efficacy and refer to the depth of z = 10 m and a simulation time of t = 100 years. The FE simulation results referring

to the real scenario where 100% of the basements that characterize the Chicago Loop reject heat into the ground can be found in Appendix Fig. 7 and Fig. 8.

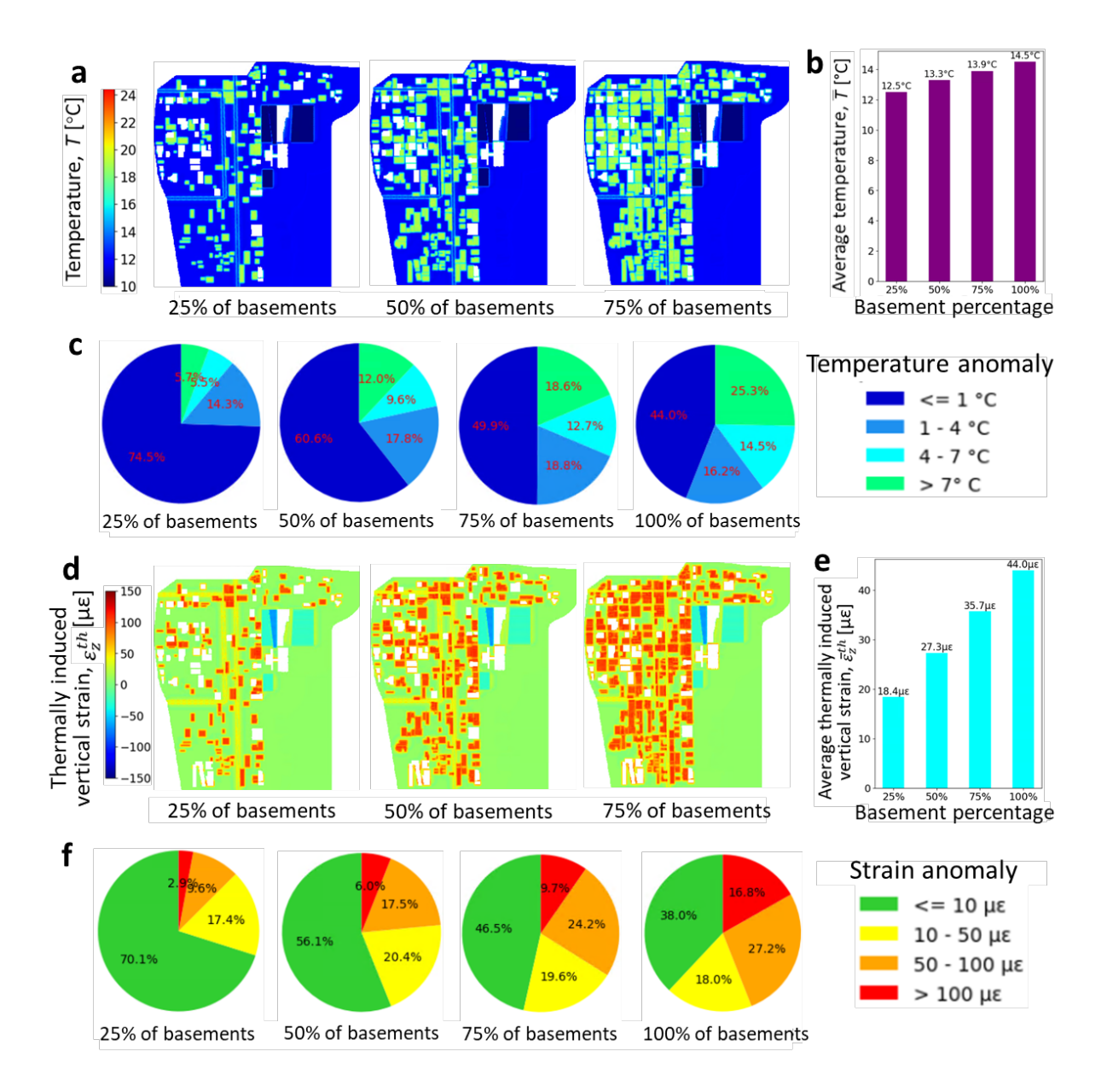


Fig. 4: Influence of basement density on ground temperature and thermally induced strains. Results refer to scenarios where 25, 50%, 75% of the basement that characterize the Chicago Loop (real case corresponding to 100% of the basements) are present and reject heat into the ground. The reference depth is of z = 10 m, the reference time is of t = 100 years, and the reference time series are of t = 1 yr, 2 yrs, 10

yrs, and 20 yrs, using training set B. (a) Predicted maps of ground temperature. (b) Average ground temperature in the considered scenarios. (c) Proportional pie chart of surface areas with threshold temperature variations compared with the initial state. (d) Predicted maps of thermally induced vertical ground strain. (e) Average vertical ground strain in the considered scenarios. (f) Proportional pie chart of surface areas with threshold thermally induced ground strains compared with the initial state.

The results shed light on one distinct effect caused by the density of underground heat sources (Fig. 4): the ground temperatures and thermally induced vertical strains increase nonlinearly with an increase in the number of heat sources. The largest temperature anomalies are found in proximity of the heat sources (Fig. 4(a)). When the number of basements increases from 25% to 100%, the average temperature of the entire area increases by 2 °C Fig. 4(b). As the Chicago Loop district has approximately 470 building basements (Rotta Loria, 2023) over an area of 1.13 km², this result corresponds to an increase in the average ground temperature per unit surface and basements of 0.0067 °C/km²/basement. A quantitative analysis of the temperature variations characterizing the studied urban district (Fig. 4(c)) further reveals that the areas where temperature anomalies exceed 7 °C is 25.3% of the total area in the real scenario where 100% of the basement reject heat into the ground, whereas this surface accounts for only 12.0% and 5.7% in the hypothetical scenarios where only 50% and 25% of the basements are present and reject heat into the ground, respectively. Comparable results are obtained for the thermally induced ground strains, with larger strains being observed closer to heat sources (Fig. 4(d)), average strain variations of 25.6 με being observed when the number of basements increases from 25% to 100% (Fig. 4(e)), and surface areas where strains are higher than 50 µE being 44% and only 12.5% of the total when 100% and 25% of the basements reject heat into the ground, respectively (Fig. 4(f)).

Overall, the results demonstrate that the density of heat sources significantly influences the intensity and extent of SUHIs. Careful consideration of this factor is required in underground space planning to mitigate or prevent the occurrence of excessive temperature anomalies.

4. Discussion

ML simulations trained with representative data over 5×5 m "urban elements" that may be identified to achieve a high-resolution characterization of SUHIs across urban areas appear capable of providing realistic estimates of the temperature and thermally induced strains in both the space and time domains. In this study, such data referred to the ground and derived from FE simulations. Nevertheless, equally satisfactory results would be obtained if other sources of data (e.g., deriving from computations or experimental measurement campaigns) were to be employed for the same purpose.

The results indicate that ground data collected around diverse heat sources over 15% of the studied area that discretize a given urban area in plan view (training dataset A) yield highly accurate ML simulation results, learning the underlying patterns that influence the thermal and mechanical responses of the subsurface. Similarly, data collected around diverse heat sources but referring to less than 1% of the elements that discretize such urban area (training dataset B) also provide accurate results, despite being affected by slightly larger errors. Notably, data collected from a single type of heat sources (e.g., building basements) and across a unique and concentrated area represented by a building block (corresponding to an even smaller percentage of the elements) provide results that are generally characterized by larger errors. However, such results become highly accurate in proximity of heat sources of the same type against which the ML simulations were trained. Therefore, in these situations, we could study underground climate change over an entire city district by leveraging a handful of data collected in the vicinity of a building block, which may be expediently obtained with computational simulations or experimental measurement campaigns.

The FE simulations employed in this work required approximately 4 hours and 56 minutes to compute the spatial and temporal variations of the temperature field over the reference area and simulation timeframe (saving results every 0.25 years). When such simulations also addressed the mechanics of the problem via a coupled thermo-mechanical formulation, the computational time increased to 8 hours and 36 minutes, requiring a memory of more than 180 GB. In contrast, ML simulations addressing the calculation of ground temperatures in the spatial domain via training sets A, B, and C required only about 21 minutes, 3 minutes, and 2 minutes and 30 seconds, hence being 14.1 times, 98.7 times, and 118.4 times faster, respectively. Additionally, ML simulations addressing the calculation of ground deformations in the spatial domain via training sets A, B, and C required approximately 25 minutes, 3 minutes and 20 seconds, and 2 minutes and 40 seconds, hence being 20.6 times, 155.0 times, and 193.5 times faster. These results illustrate the robust advantages of ML to save computational time and resources.

The proposed ML approach also appears to have advantages in terms of efficiency compared to one recent endeavor to model SUHIs through statistical clustering methods, focusing on temperature anomalies and not thermally induced ground deformations (Kreitmair et al., 2023). In our study, simulations were performed using an Intel(R) Xeon(R) Processor E5-2699 v4 (2.20 GHz, 22 cores), while the referenced study used an Intel(R) Xeon(R) Silver 4116 Processor (2.10 GHz, 12 cores). Based on the consideration that "Theoretical computational speed = number of cores × base clock frequency", the former is theoretically 92% faster than the latter, involving that a task taking 60 minutes on the E5-2699 v4 would take approximately 115 minutes on the Silver 4116. In the referenced study (Kreitmair et al., 2023), temperature calculations with three modeling options required 54 hours, 24 hours, and some minutes, respectively, which would correspond to approximately 27 hours, 12 hours, and a few minutes with our computational resources. Considering that the area investigated in the referenced study (Kreitmair et al., 2023) was approximately 7.5 times larger than the Chicago Loop, and assuming a simplistic linear relationship between calculation time and area size, the time required to model an urban area similar to the Loop using the method from the referenced study would be approximately 3.6 hours, 1.6 hours, and a few

seconds. Notably, these simulation times are still longer than those achieved in the present work for datasets A and B (where our analyses using the RF model required only about 21 minutes and 3 minutes, respectively) and may only be comparable to those obtained with dataset C. Therefore, it can be concluded that the method proposed here is overall more efficient than the state-of-the-art.

The proposed ML approach may also be employed to quantify other essential variables for the characterization of SUHIs, including direct quantifications of ground displacements and indirect quantifications of waste heat rejected into the ground. Additionally, the physically based features selected to inform the ML algorithm proposed in this work would enable the study, simulation, and prediction of the intensity and evolution of SUHIs in general urban areas, and the expedient and accurate creation of 2-D and 3-D visualizations of central effects of such phenomena. For instance, this information would allow to identify "hot spots" in the subsurface of cities where SUHIs are particularly intense, as well as to predict the future evolution of SUHIs as a function of variable urban patterns (e.g., variations in the density of heat sources due to the construction and demolition of buildings) – the holy grail of current computational approaches to explore SUHIs. By rapidly identifying hot spots in underground spaces, the findings of this work can serve two principal actions: (1) enhance urban sustainability by implementing geothermal technologies to absorb waste heat for use in buildings and district-scale energy networks; and/or (2) identifying underground constructions that may particularly benefit from retrofit interventions (consisting of thermal insulations of underground building enclosures) dedicated to minimize waste heat emissions.

4. Concluding remarks

The results of this work reveal that ML simulations enable the study, simulation, and prediction of SUHIs with outstanding accuracy and efficiency, hence representing a powerful alternative or complementary resource to established yet daunting computational approaches. With its advanced capabilities, the proposed ML approach serves as a powerful tool to not only support scientific investigations but also advance

engineering solutions and urban planning strategies dedicated to mitigating underground climate change. Broadly, this work introduces a previously unavailable computational approach to studying a central phenomenon in subsurface climatology, geothermal energy, environmental science, hydrogeology, transportation engineering, and civil engineering: the temporal spread of heat around underground sources with arbitrary geometries and its impacts on the subsurface.

Appendix A

The figures showing computation results for all case studies in Sections 3.1 and 3.2, along with the errors for all case studies in Section 3.1, are presented in this appendix.

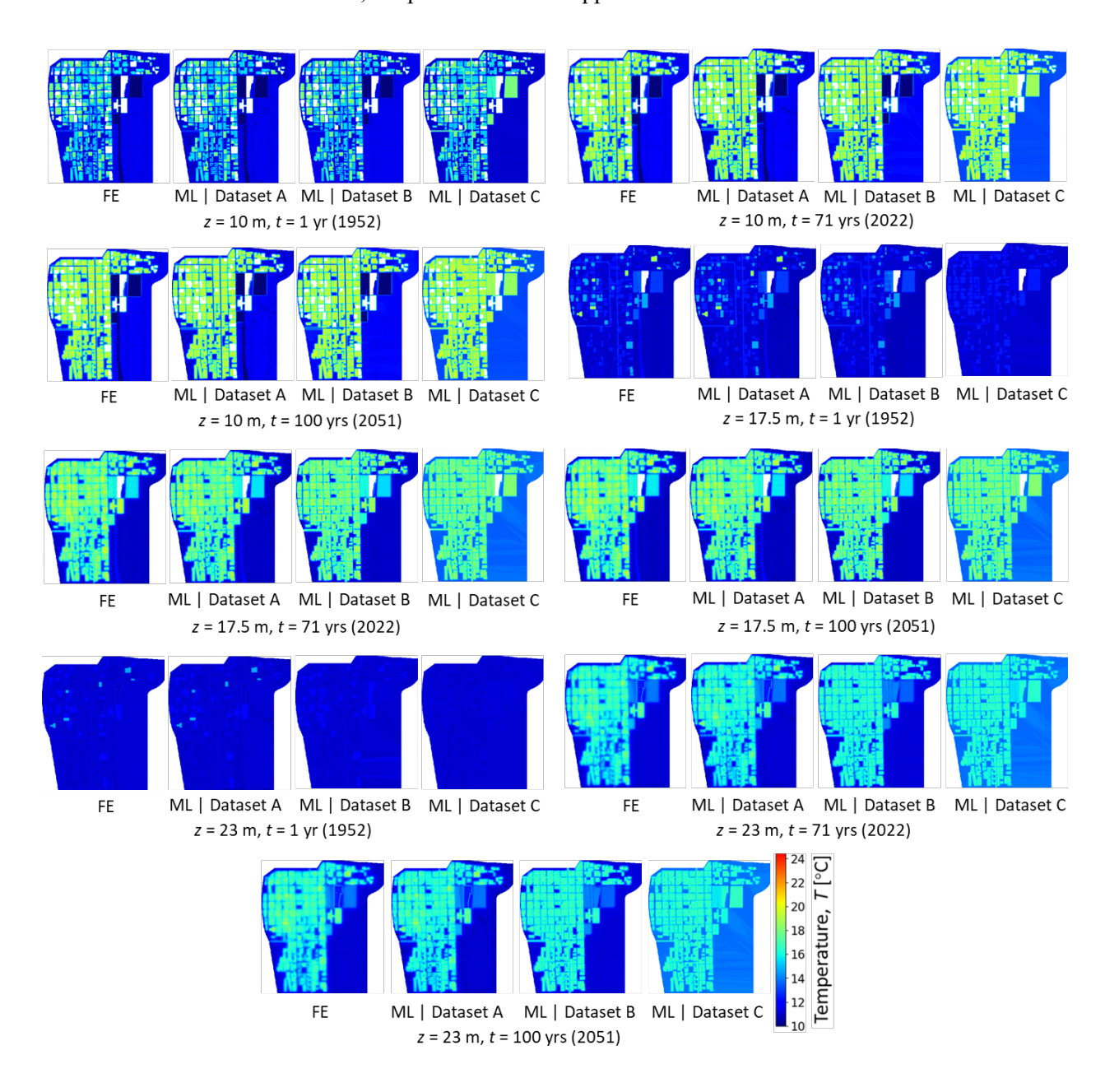


Fig. 5: Temperature maps in the space domain obtained from the ML and FE simulations. Results are based on training sets A, B, and C. They refer to the three reference depths of 10 m, 17.5 m, and 23 m

and the three reference simulation times of 1 year, 71 years, and 100 years (corresponding to the years 1952, 2022, and 2051, respectively).

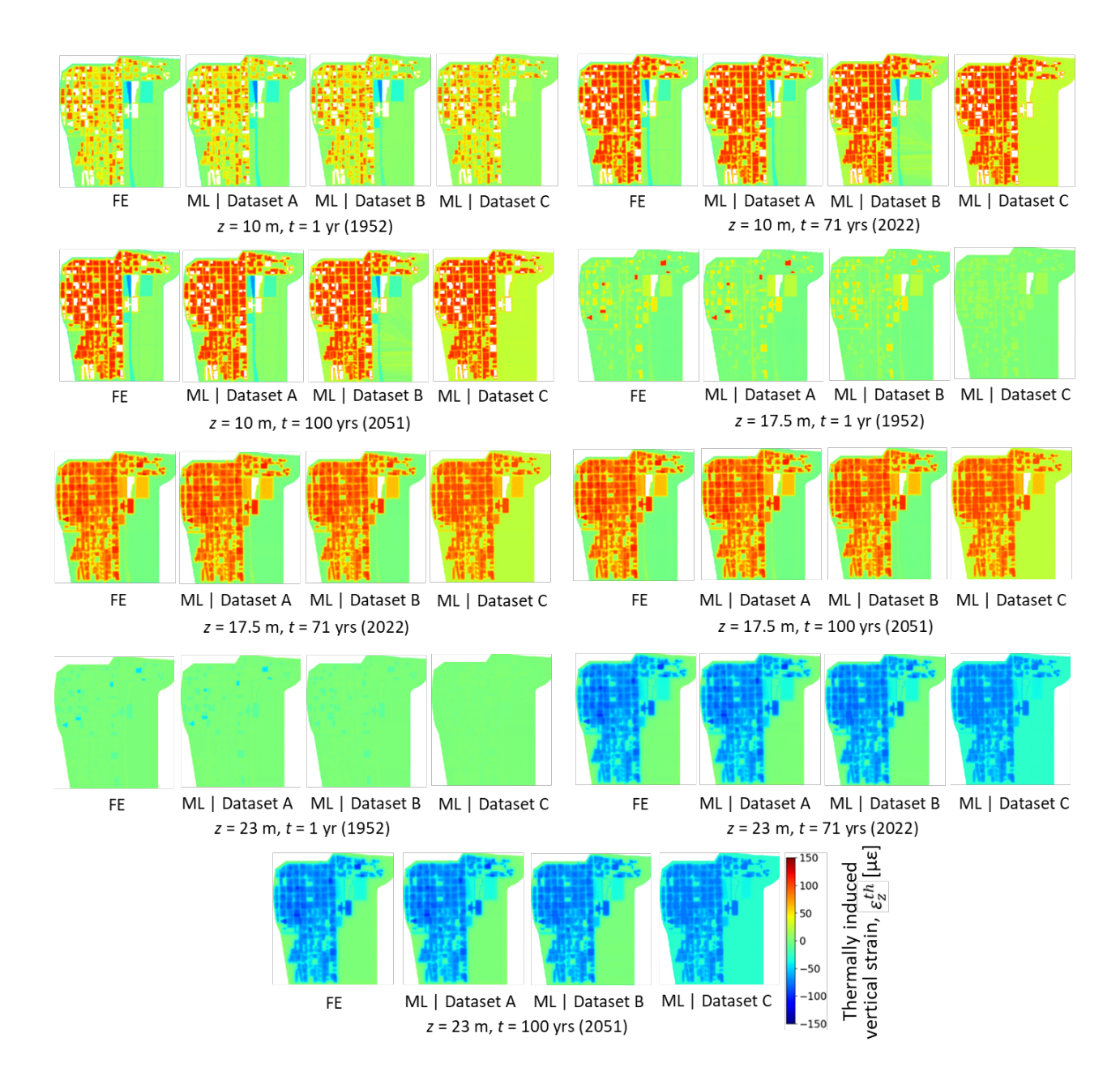


Fig. 6: Strain maps in the space domain obtained from the ML and FE simulations. Results are based on training sets A, B, and C. They refer to the three reference depths of 10 m, 17.5 m, and 23 m and the

three reference simulation times of 1 year, 71 years, and 100 years (corresponding to the years 1952, 2022, and 2051, respectively).

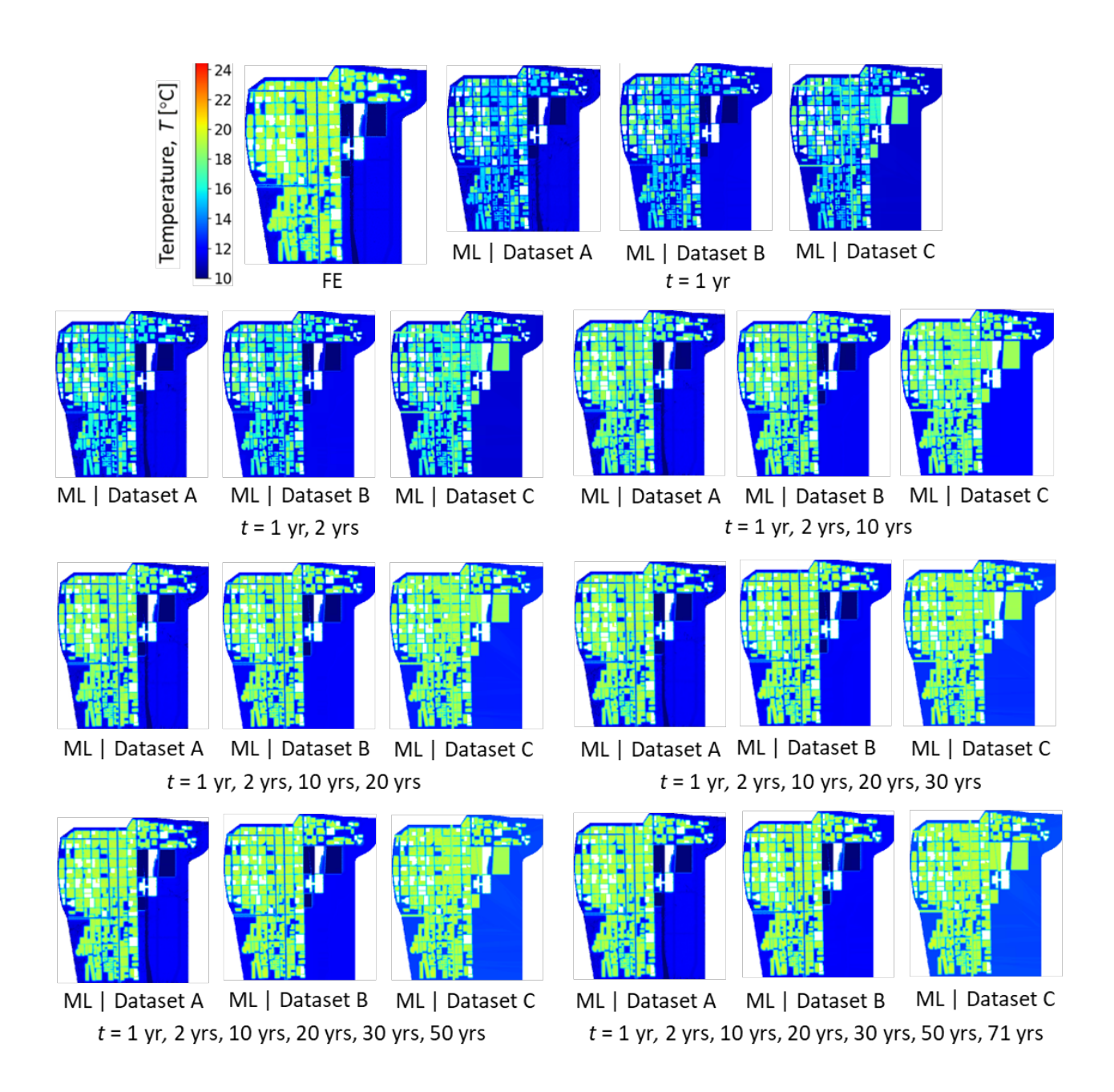


Fig. 7: Temperature maps in the time domain obtained from the ML and FE simulations. Results are based on training sets A, B, and C and consider the seven selected time sets reported in Table 3. Predictions are made with reference to the simulation time of 100 years (corresponding to 2051) and the depth of 10 m.

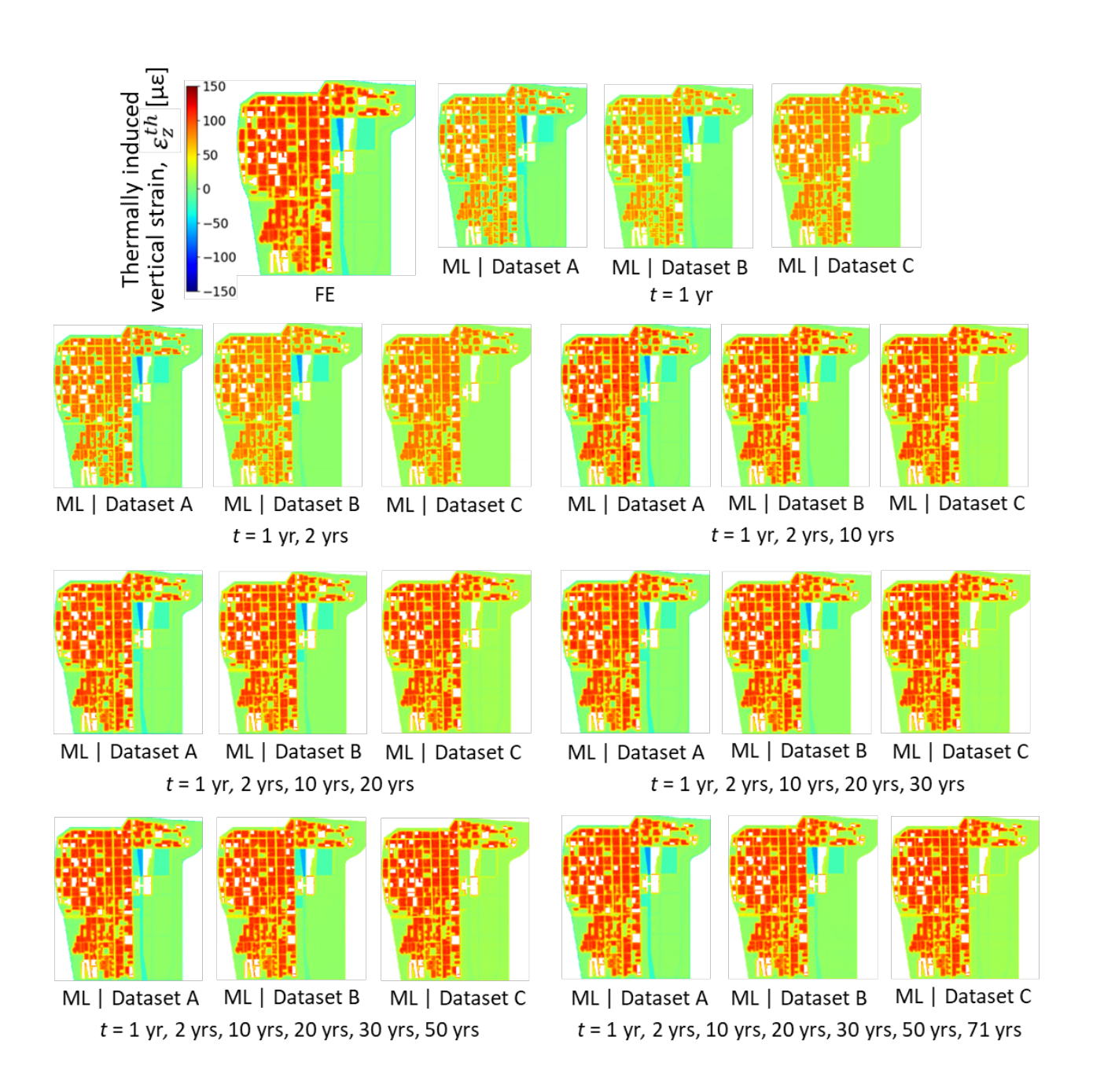


Fig. 8: Strain maps in the time domain obtained from the ML and FE simulations. Results are based on training sets A, B, and C and consider the seven selected time sets reported in Table 3. Predictions are made with reference to the simulation time of 100 years (corresponding to 2051) and the depth of 10 m.

Table 4: MAE and R^2 of temperature obtained in the space domain using different training sets.

Studied cases	MAE of temperature (°C)			R^2 of temperature		
Studied Cases	Set A	Set B	Set C	Set A	Set B	Set C
z = 10 m, t = 1 yr	0.28	0.37	0.63	0.92	0.86	0.31
z = 10 m, t = 71 yrs	0.28	0.46	0.99	0.95	0.90	0.45
z = 10 m, t = 100 yrs	0.28	0.45	1.00	0.95	0.91	0.46
z = 17.5 m, t = 1 yr	0.23	0.44	0.78	0.83	0.63	0.35
z = 17.5 m, t = 71 yrs	0.34	0.62	0.95	0.96	0.91	0.63
z = 17.5 m, t = 100 yrs	0.34	0.64	0.94	0.96	0.91	0.63
z = 23 m, t = 1 yr	0.12	0.20	0.27	0.50	0.15	0.03
z = 23 m, t = 71 yrs	0.28	0.53	1.07	0.94	0.86	0.37
z = 23 m, t = 100 yrs	0.30	0.57	1.01	0.94	0.87	0.36

Table 5: MAE and R^2 of strain obtained in the space domain using different training sets.

Studied cases	MAI	E of strain	(με)	R^2 of strain			
Studied cases	Set A	Set B	Set C	Set A	Set B	Set C	
z = 10 m, t = 1 yr	3.5	6.4	6.8	0.98	0.93	0.78	
z = 10 m, t = 71 yrs	3.2	6.3	6.8	0.99	0.95	0.78	
z = 10 m, t = 100 yrs	3.2	6.3	6.8	0.99	0.95	0.77	

z = 17.5 m, t = 1 yr	1.3	3.5	12.6	0.99	0.74	0.36
z = 17.5 m, t = 71 yrs	1.2	2.1	3.1	1.00	0.97	0.82
z = 17.5 m, t = 100 yrs	1.2	2.2	3.1	1.00	0.97	0.82
z = 23 m, t = 1 yr	0.5	4.0	12.4	0.99	0.46	0.20
z = 23 m, t = 71 yrs	0.6	1.4	3.3	1.00	0.98	0.65
z = 23 m, t = 100 yrs	0.6	1.5	3.4	1.00	0.98	0.63

References

- Alberto, P., & Crosta, G. B. (2021). Characterization of the subsurface urban heat island and its sources in the Milan city area, Italy. *Hydrogeology Journal*, 29(7), 2487–2500. https://doi.org/10.1007/s10040-021-02387-z
- Amato, F., Guignard, F., Robert, S., & Kanevski, M. (2020). A novel framework for spatio-temporal prediction of environmental data using deep learning. *Scientific Reports*, 10(1), 22243. https://doi.org/10.1038/s41598-020-79148-7
- Bayer, P., Attard, G., Blum, P., & Menberg, K. (2019). The geothermal potential of cities. *Renewable and Sustainable Energy Reviews*, 106, 17–30. https://doi.org/10.1016/j.rser.2019.02.019
- Bayer, P., Rivera, J. A., Schweizer, D., Schärli, U., Blum, P., & Rybach, L. (2016). Extracting past atmospheric warming and urban heating effects from borehole temperature profiles. *Geothermics*, 64, 289–299. https://doi.org/10.1016/j.geothermics.2016.06.011
- Benz, S. A., Bayer, P., Goettsche, F. M., Olesen, F. S., & Blum, P. (2016). Linking Surface Urban Heat Islands with Groundwater Temperatures. *Environmental Science & Technology*, 50(1), 70–78. https://doi.org/10.1021/acs.est.5b03672
- Benz, S. A., Menberg, K., Bayer, P., & Kurylyk, B. L. (2022). Shallow subsurface heat recycling is a sustainable global space heating alternative. *Nature Communications*, *13*(1), Article 1. https://doi.org/10.1038/s41467-022-31624-6
- Bidarmaghz, A., Choudhary, R., Soga, K., Kessler, H., Terrington, R. L., & Thorpe, S. (2019). Influence of geology and hydrogeology on heat rejection from residential basements in urban areas.

 Tunnelling and Underground Space Technology, 92, 103068.

 https://doi.org/10.1016/j.tust.2019.103068
- Böttcher, F., & Zosseder, K. (2022). Thermal influences on groundwater in urban environments A multivariate statistical analysis of the subsurface heat island effect in Munich. *Science of The Total Environment*, 810, 152193. https://doi.org/10.1016/j.scitotenv.2021.152193

- Breiman, L. (2001). Random Forests. *Machine Learning*, 45(1), 5–32. https://doi.org/10.1023/A:1010933404324
- Cassina, L., Laloui, L., & Rotta Loria, A. F. (2022). Thermal interactions among vertical geothermal borehole fields. *Renewable Energy*, *194*, 1204–1220. https://doi.org/10.1016/j.renene.2022.05.148
- Clinton, N., & Gong, P. (2013). MODIS detected surface urban heat islands and sinks: Global locations and controls. *Remote Sensing of Environment*, 134, 294–304. https://doi.org/10.1016/j.rse.2013.03.008
- Debbage, N., & Shepherd, J. M. (2015). The urban heat island effect and city contiguity. *Computers, Environment and Urban Systems*, 54, 181–194. https://doi.org/10.1016/j.compenvurbsys.2015.08.002
- Epting, J., & Huggenberger, P. (2013). Unraveling the heat island effect observed in urban groundwater bodies Definition of a potential natural state. *Journal of Hydrology*, 501, 193–204. https://doi.org/10.1016/j.jhydrol.2013.08.002
- Ferguson, G., & Woodbury, A. D. (2007). Urban heat island in the subsurface. *Geophysical Research Letters*, *34*(23). https://doi.org/10.1029/2007GL032324
- Gobakis, K., Kolokotsa, D., Synnefa, A., Saliari, M., Giannopoulou, K., & Santamouris, M. (2011).

 Development of a model for urban heat island prediction using neural network techniques.

 Sustainable Cities and Society, 1(2), 104–115. https://doi.org/10.1016/j.scs.2011.05.001
- Hastie, T., Tibshirani, R., & Friedman, J. (2009). *The Elements of Statistical Learning*. Springer. https://doi.org/10.1007/978-0-387-84858-7
- Heaviside, C., Macintyre, H., & Vardoulakis, S. (2017). The Urban Heat Island: Implications for Health in a Changing Environment. *Current Environmental Health Reports*, 4(3), 296–305. https://doi.org/10.1007/s40572-017-0150-3

- Hemmerle, H., Hale, S., Dressel, I., Benz, S. A., Attard, G., Blum, P., & Bayer, P. (2019). Estimation of Groundwater Temperatures in Paris, France. *Geofluids*, 2019, e5246307. https://doi.org/10.1155/2019/5246307
- Ho, T. K. (1995). Random decision forests. *Proceedings of 3rd International Conference on Document Analysis and Recognition*, 1, 278–282 vol.1. https://doi.org/10.1109/ICDAR.1995.598994
- Huang, F., Zhan, W., Wang, Z.-H., Voogt, J., Hu, L., Quan, J., Liu, C., Zhang, N., & Lai, J. (2020). Satellite identification of atmospheric-surface-subsurface urban heat islands under clear sky. *Remote Sensing of Environment*, 250, 112039. https://doi.org/10.1016/j.rse.2020.112039
- Jenkins, K., Gilbey, M., Hall, J., Glenis, V., & Kilsby, C. (2014). Implications of climate change for thermal discomfort on underground railways. *Transportation Research Part D: Transport and Environment*, 30, 1–9. https://doi.org/10.1016/j.trd.2014.05.002
- Kafy, A.-A., Abdullah-Al-Faisal, Rahman, Md. S., Islam, M., Al Rakib, A., Islam, Md. A., Khan, Md. H.
 H., Sikdar, Md. S., Sarker, Md. H. S., Mawa, J., & Sattar, G. S. (2021). Prediction of seasonal urban thermal field variance index using machine learning algorithms in Cumilla, Bangladesh.
 Sustainable Cities and Society, 64, 102542. https://doi.org/10.1016/j.scs.2020.102542
- Kalnay, E., & Cai, M. (2003). Impact of urbanization and land-use change on climate. *Nature*, 423(6939), Article 6939. https://doi.org/10.1038/nature01675
- Knorr, W., Prentice, I. C., House, J. I., & Holland, E. A. (2005). Long-term sensitivity of soil carbon turnover to warming. *Nature*, *433*(7023), Article 7023. https://doi.org/10.1038/nature03226
- Kreitmair, M. J., Makasis, N., Bidarmaghz, A., Menberg, K., Choudhary, R., & Soga, K. (2023). Finding common ground: A methodology for city-scale subsurface thermal modelling. *Urban Climate*, 49, 101513. https://doi.org/10.1016/j.uclim.2023.101513
- Laloui, L. (2001). Thermo-mechanical behaviour of soils. *Revue Française de Génie Civil*, 5, 809–843. https://doi.org/10.1080/12795119.2001.9692328

- Lokoshchenko, M. A., & Korneva, I. A. (2015). Underground urban heat island below Moscow city. *Urban Climate*, *13*, 1–13. https://doi.org/10.1016/j.uclim.2015.04.002
- Luo, Z., & Asproudi, C. (2015). Subsurface urban heat island and its effects on horizontal ground-source heat pump potential under climate change. *Applied Thermal Engineering*, 90, 530–537. https://doi.org/10.1016/j.applthermaleng.2015.07.025
- Lyu, F., Wang, S., Han, S. Y., Catlett, C., & Wang, S. (2022). An integrated cyberGIS and machine learning framework for fine-scale prediction of Urban Heat Island using satellite remote sensing and urban sensor network data. *Urban Informatics*, 1(1), 6. https://doi.org/10.1007/s44212-022-00002-4
- Menberg, K., Bayer, P., Zosseder, K., Rumohr, S., & Blum, P. (2013). Subsurface urban heat islands in German cities. *Science of The Total Environment*, 442, 123–133. https://doi.org/10.1016/j.scitotenv.2012.10.043
- Müller, N., Kuttler, W., & Barlag, A.-B. (2014). Analysis of the subsurface urban heat island in Oberhausen, Germany. *Climate Research*, *58*(3), 247–256. https://doi.org/10.3354/cr01195
- Mushore, T. D., Odindi, J., Dube, T., & Mutanga, O. (2017). Prediction of future urban surface temperatures using medium resolution satellite data in Harare metropolitan city, Zimbabwe. *Building and Environment*, 122, 397–410. https://doi.org/10.1016/j.buildenv.2017.06.033
- Noethen, M., Hemmerle, H., & Bayer, P. (2023). Sources, intensities, and implications of subsurface warming in times of climate change. *Critical Reviews in Environmental Science and Technology*, 53(5), 700–722. https://doi.org/10.1080/10643389.2022.2083899
- Noethen, M., Hemmerle, H., Menberg, K., Epting, J., Benz, S. A., Blum, P., & Bayer, P. (2023). Thermal impact of underground car parks on urban groundwater. *Science of The Total Environment*, 903, 166572. https://doi.org/10.1016/j.scitotenv.2023.166572
- Oke, T. R., Mills, G., Christen, A., & Voogt, J. A. (2017). *Urban Climates*. Cambridge University Press. https://doi.org/10.1017/9781139016476

- Papantoniou, S., & Kolokotsa, D.-D. (2016). Prediction of outdoor air temperature using neural networks:

 Application in 4 European cities. *Energy and Buildings*, 114, 72–79.

 https://doi.org/10.1016/j.enbuild.2015.06.054
- Previati, A., Epting, J., & Crosta, G. B. (2022). The subsurface urban heat island in Milan (Italy)—A modeling approach covering present and future thermal effects on groundwater regimes. *Science of The Total Environment*, 810, 152119. https://doi.org/10.1016/j.scitotenv.2021.152119
- Rizwan, A. M., Dennis, L. Y. C., & Liu, C. (2008). A review on the generation, determination and mitigation of Urban Heat Island. *Journal of Environmental Sciences*, 20(1), 120–128. https://doi.org/10.1016/S1001-0742(08)60019-4
- Robinson, S. I., McLaughlin, Ó. B., Marteinsdóttir, B., & O'Gorman, E. J. (2018). Soil temperature effects on the structure and diversity of plant and invertebrate communities in a natural warming experiment. *Journal of Animal Ecology*, 87(3), 634–646. https://doi.org/10.1111/1365-2656.12798
- Rotta Loria, A. F. (2023). The silent impact of underground climate change on civil infrastructure.

 *Communications Engineering, 2(1), Article 1. https://doi.org/10.1038/s44172-023-00092-1
- Rotta Loria, A. F., & Coulibaly, J. B. (2021). Thermally induced deformation of soils: A critical overview of phenomena, challenges and opportunities. *Geomechanics for Energy and the Environment*, 25, 100193. https://doi.org/10.1016/j.gete.2020.100193
- Rotta Loria, A. F., Thota, A., Thomas, A. M., Friedle, N., Lautenberg, J. M., & Song, E. C. (2022). Subsurface heat island across the Chicago Loop district: Analysis of localized drivers. *Urban Climate*, 44(101211), 1–25.
- Schweighofer, J. A. V., Wehrl, M., Baumgärtel, S., & Rohn, J. (2021). Detecting Groundwater Temperature

 Shifts of a Subsurface Urban Heat Island in SE Germany. *Water*, *13*(10), Article 10.

 https://doi.org/10.3390/w13101417

- Shi, B., Tang, C.-S., Gao, L., Liu, C., & Wang, B.-J. (2012). Observation and analysis of the urban heat island effect on soil in Nanjing, China. *Environmental Earth Sciences*, 67(1), 215–229. https://doi.org/10.1007/s12665-011-1501-2
- Taniguchi, M., Uemura, T., & Jago-on, K. (2007). Combined Effects of Urbanization and Global Warming on Subsurface Temperature in Four Asian Cities. *Vadose Zone Journal*, *6*(3), 591–596. https://doi.org/10.2136/vzj2006.0094
- Visser, P. W., Kooi, H., Bense, V., & Boerma, E. (2020). Impacts of progressive urban expansion on subsurface temperatures in the city of Amsterdam (The Netherlands). *Hydrogeology Journal*, 28(5), 1755–1772. https://doi.org/10.1007/s10040-020-02150-w
- Yuan, F., & Bauer, M. E. (2007). Comparison of impervious surface area and normalized difference vegetation index as indicators of surface urban heat island effects in Landsat imagery. *Remote Sensing of Environment*, 106(3), 375–386. https://doi.org/10.1016/j.rse.2006.09.003
- Zhan, W., Ju, W., Hai, S., Ferguson, G., Quan, J., Tang, C., Guo, Z., & Kong, F. (2014). Satellite-Derived Subsurface Urban Heat Island. *Environmental Science & Technology*, 48(20), 12134–12140. https://doi.org/10.1021/es5021185
- Zhou, D., Xiao, J., Bonafoni, S., Berger, C., Deilami, K., Zhou, Y., Frolking, S., Yao, R., Qiao, Z., & Sobrino, J. A. (2019). Satellite Remote Sensing of Surface Urban Heat Islands: Progress, Challenges, and Perspectives. *Remote Sensing*, 11(1), Article 1. https://doi.org/10.3390/rs11010048
- Zhou, Z.-H. (2021). *Machine Learning*. Springer Nature.
- Zhu, K., Blum, P., Ferguson, G., Balke, K.-D., & Bayer, P. (2010). The geothermal potential of urban heat islands. *Environmental Research Letters*, 5(4), 044002. https://doi.org/10.1088/1748-9326/5/4/044002

Zumwald, M., Knüsel, B., Bresch, D. N., & Knutti, R. (2021). Mapping urban temperature using crowdsensing data and machine learning. *Urban Climate*, *35*, 100739. https://doi.org/10.1016/j.uclim.2020.100739